ELSEVIER

Rayleigh–Taylor instability as a mechanism for corona formation on Venus

Trudi Hoogenboom *, Gregory A. Houseman

School of Earth Sciences, University of Leeds, Leeds, LS2 9JT, UK

Abstract

In this study we explore the idea that coronae have formed on Venus as a result of gravitational (Rayleigh–Taylor) instability of the lithosphere. The lithosphere is represented by a system of stratified homogeneous viscous layers (low-density crust over high density mantle, over lower density layer beneath the lithosphere). A small harmonic perturbation imposed on the base of the lithosphere is observed to result in gravitational instability under the constraint of assumed axisymmetry. Topography develops with time under the influence of dynamic stress associated with downwelling or upwelling, and spatially variable crustal thickening or thinning. Topography may therefore be elevated or depressed above a mantle downwelling, but the computed gravity anomaly is always negative above a mantle downwelling in a homogeneous asthenosphere. The ratio of peak gravity to topography anomaly depends primarily on the ratio of crust to lithospheric viscosity. Average observed ratios are well resolved for two groups of coronae ($\sim$40 mgal km^{-1}), consistent with models in which the crust is perhaps 5 times stronger than the lithosphere. Group 3a (rim surrounding elevated central region) coronae are inferred to arise from a central upwelling model, whereas Group 8 (depression) coronae are inferred to arise from central downwelling. Observed average coronae radii are consistent with a lithospheric thickness of only 50 km. An upper low-density crustal layer is 10–20 km thick, as inferred from the amplitude of gravity and topography anomalies.
© 2005 Elsevier Inc. All rights reserved.

Keywords: Venus

1. Introduction

Coronae are quasi-circular volcano-tectonic features that range in diameter from $\sim$75 km to over 1000 km (e.g. Fig. 1) and are considered unique to Venus. Coronae are generally believed to form over small-scale mantle upwellings or plumes (Stofan et al., 1991; Squyres et al., 1992; Janes et al., 1992).

The most successful model of corona formation predicts the range of observed topographic signatures using a model in which plume-like mantle upwellings cause the cold, dense lower lithosphere to delaminate, sinking into the mantle and deforming the surface (Smrekar and Stofan, 1997). This model can account for the majority of tectonic deformation, however some questions remain unanswered. The size and depth at which the assumed mantle plumes originate is unclear, and the relatively close spacing of many coronae is surprising if

these plumes originate from deep in the mantle. The size and spacing of coronae imply relatively small plumes, but small plumes originating at the core–mantle boundary could be thermally assimilated in the mantle (Hansen, 2003). In addition, mantle upwelling models fail to address the relative lack of volcanism noted at some coronae.

Here we explore an alternative causal mechanism for coronae, based on gravitational (Rayleigh–Taylor) instability of the lithosphere (Tackley and Stevenson, 1991; Tackley et al., 1992). Rayleigh–Taylor (R–T) instability may occur when a layer of dense fluid (i.e. lithosphere) overlies a layer of less dense fluid (asthenosphere). Under such conditions, small deflections of the boundary between the two fluids grow until the system overturns (Chandrasekhar, 1961). The lithosphere may be unstable relative to the underlying layer because it is colder and therefore denser. Although terrestrial lithosphere is depleted in old cratonic regions (e.g. Jordan, 1978) and its chemical composition implies intrinsic buoyancy that increases with age (Poudjom-Djomani et al., 2001), it is likely that the continental lithosphere is denser in many younger regions (Houseman and Molnar,

* Corresponding author. Jet Propulsion Laboratory, 4800 Oak Grove Drive, Mail Stop 183-501, Pasadena, CA 91109, USA.

E-mail addresses: trudi@jpl.nasa.gov (T. Hoogenboom), greg@earth.leeds.ac.uk (G.A. Houseman).
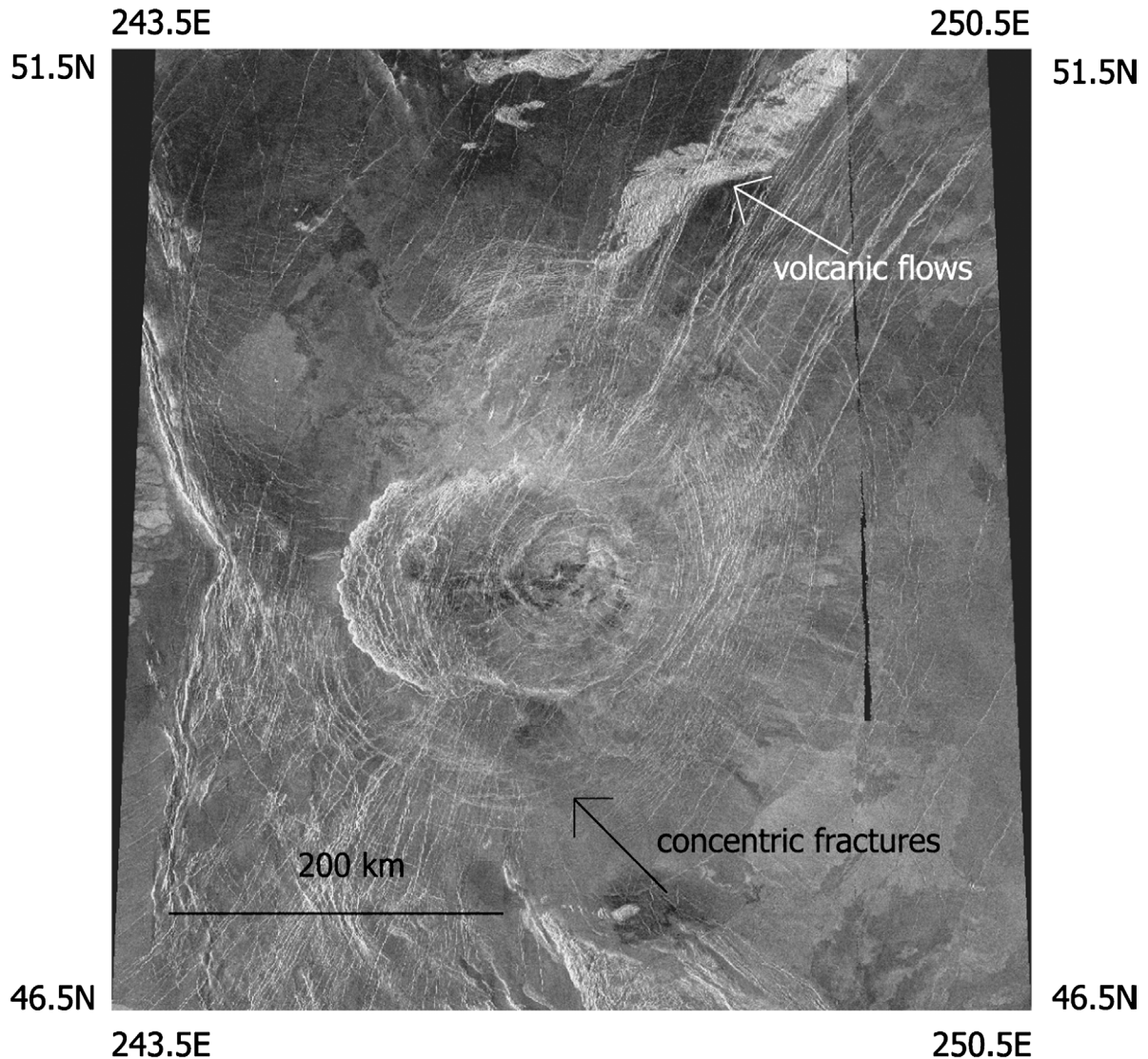
Fig. 1. Magellan synthetic aperture radar image of Nalwomga corona (48.7° N, 247° E). Nalwomga is a concentric, depression-shaped corona (380 km in diameter) located in the plains. Black regions indicate data gaps. Image from http://pdsmaps.wr.usgs.gov.

1997, 2001). Venus and Earth are similar in size and mass and therefore should have a similar bulk composition despite the apparent absence of water on Venus (Kaula, 1999). Conductive cooling and the likelihood of lesser chemical depletion therefore lead us to expect that the venusian lithosphere is similarly denser than the underlying layer, at least in some regions.

Various aspects of the R–T mechanism including non-Newtonian viscosity (Houseman and Molnar, 1997), stratification of density and viscosity (Molnar et al., 1998), the effects of a crustal layer (Neil and Houseman, 1999), or externally forced convergence (Billen and Houseman, 2004) have previously been quantified. Pysklywec and Beaumont (2004) described the asymmetric evolution of the instability when the upper layers deform plastically. All of those studies were based on 2D plane-strain calculations in the context of the Earth. Here we consider the development of R–T instability under the assumption of 2D axisymmetry. In experimental R–T systems, instabilities that grow from background noise always produce a cluster of localised approximately axisymmetric blobs (Whitehead and

Luther, 1975). In any case, ~80% of coronae are approximately axisymmetric (Stofan et al., 1992).

Magellan topography and free-air gravity data have recently been used (e.g. Hoogenboom et al., 2004), to constrain models of the venusian lithosphere where coronae have formed, assuming an elastic layer that flexes under the load associated with corona formation. Such models help us to understand where the load is applied, but do not explain the mechanism that causes the load. It is clear from structural interpretations (e.g. Copp et al., 1998), that corona formation is associated with pervasive and permanent deformation. Deformation of a low-density crustal layer is a natural outcome of R–T instability of the underlying lithospheric mantle, as shown for 2D plane-strain by Neil and Houseman (1999). Here we calculate deformation of the crust caused by instability of the mantle layer where axisymmetry is imposed, and use gravity and topography observations to constrain model parameters. Our model may be contrasted with the plume/delamination model of Smrekar and Stofan (1997) in which plumes originating at depth are required

to drive the formation of coronae. The primary difference is that here, deformation is driven by an instability that develops locally within the lithosphere.

2. Methods

2.1. Governing equations and solution method

The inertial terms are negligible in the balance of stress for creeping viscous flow. Conservation of momentum in cylindrical coordinates (Malvern, 1969) describes the balance between body force, viscous stress and pressure gradients:

$$\frac{\partial (r\sigma_{rr})}{\partial r} + \frac{\partial (r\sigma_{rz})}{\partial z} - \sigma_{\theta\theta} = 0, \tag{1a}$$

$$\frac{\partial (r\sigma_{rz})}{\partial r} + \frac{\partial (r\sigma_{zz})}{\partial z} = r\rho g, \tag{1b}$$

where σ is the stress, ρ is the density, g is the acceleration due to gravity (acting in the negative z direction), and r is the radial co-ordinate, and we have assumed that the solution does not vary in the tangential (θ) direction. The stress (σ_{ij}) may be resolved into pressure (P) and deviatoric stress (τ_{ij}) according to

$$\sigma_{ij} = P\delta_{ij} + \tau_{ij}, \tag{2}$$

where δ_{ij} is the Kronecker delta. A Newtonian constitutive relation between deviatoric stress (τ_{ij}) and strain-rate ($\dot{\varepsilon}_{ij}$) is assumed:

$$\tau_{ij} = 2\eta \dot{\varepsilon}_{ij}, \tag{3}$$

where η is the viscosity. For axisymmetric flow, the strain rates are defined in terms of the radial (u) and vertical (v) velocity components:

$$\dot{\varepsilon}_{rr} = \frac{\partial u}{\partial r}, \tag{4a}$$

$$\dot{\varepsilon}_{\theta\theta} = \frac{u}{r}, \tag{4b}$$

$$\dot{\varepsilon}_{zz} = \frac{\partial v}{\partial z}, \tag{4c}$$

$$\dot{\varepsilon}_{rz} = \frac{1}{2}\left(\frac{\partial u}{\partial z} + \frac{\partial v}{\partial r}\right). \tag{4d}$$

The velocity field is assumed incompressible under conditions of cylindrical axisymmetry:

$$\frac{\partial}{\partial r}(ru) + \frac{\partial}{\partial z}(rv) = 0. \tag{5}$$

For a given density and viscosity distribution, and appropriate boundary conditions, the flow field in the form of velocity components $u(r, z)$, $v(r, z)$, and pressure $P(r, z)$ can be obtained by solving Eqs. (1)–(5) using the finite-element method. In order to compute finite deformation, material point coordinates (R, Z) (and properties like density and viscosity) are advected by the flow, according to

$$\frac{dR}{dt} = u, \qquad \frac{dZ}{dt} = v \tag{6}$$

which are integrated forward in time.

Numerical solutions of Eqs. (1)–(6) are obtained using a modified version of the finite-element program *basil* developed by Houseman et al. (2002). The velocity field is represented using quadratic interpolation functions on a triangular mesh. The pressure field is represented using linear interpolation functions, following Yamada et al. (1975). The set of linear equations (which results from the application of the Galerkin method to the numerical solution) is solved using the conjugate gradient method. Equation (6) is integrated using a two-step (second-order accurate) Runge–Kutta integration scheme. In these calculations the horizontal extent of the solution domain is small relative to the radius of the planet, so we neglect curvature of the surface layers. We assume that material properties (viscosity, density) are piecewise constant, and the discontinuities in these properties fall on element boundaries in the triangular mesh used by *basil*.

To validate the axisymmetric finite-element solutions, the early growth-rate of the instability, calculated from linear theory and valid for small deflections of the interfaces, was compared with the growth-rate calculated using the *basil* program. For a given wavenumber the theoretical growth rates are identical for 2D plane-strain (e.g. Neil and Houseman, 1999) and for axisymmetry; the horizontal variation is described using cosine functions for the former and Bessel functions for the latter.

2.2. Model description and boundary conditions

The model lithosphere (Fig. 2) includes a uniform crust (initially between $z = 0$ and $z = -m$, with density ρ_c, thickness m and viscosity η_c) that overlies a uniform mantle (initially between $z = -m$ and $z = -h$, with density ρ_m, thickness ($h - m$), and viscosity η_m). The lithosphere (of total thickness h) overlies asthenosphere represented by a uniform half-space of density ρ_a, and viscosity η_a small relative to η_m. The density difference between the lithosphere and the asthenosphere ($\Delta\rho$) is attributed to the difference in mean temperature and the effect of thermal expansion (though compositional differences may also contribute) (Houseman and Molnar, 1997). The calcula-
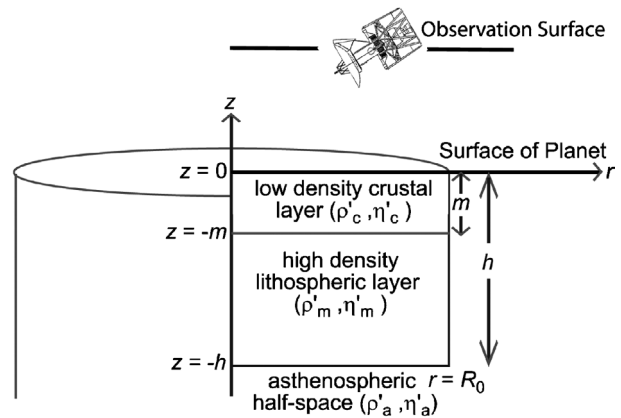

Fig. 2. Sketch of the cylindrically symmetric system of viscous fluid layers with parameters as defined in the text, for domain $r < R_0$ where kR_0 is either the first or second zero of the Bessel function J_1. The perimeter $r = R_0$ is a free-slip or reflection boundary for the purposes of these calculations.

tions ignore the variation of density and viscosity within each layer, and assume that the viscosity of the asthenosphere is negligible ($<1/10$ of the viscosity of the lithosphere). Molnar et al. (1998) and Conrad and Molnar (1997) previously quantified the effect of these approximations. The effect of thermal diffusion is also neglected under the assumption that the instability develops quickly compared to the diffusive timescale of the lithosphere.

The upper surface of the planet is approximately stress-free. For computational stability, however, we assume, as is conventional, that the vertical component of velocity on the upper boundary ($z = 0$) is zero ($v = 0$). The requirement of zero vertical traction is then satisfied by assuming that a small deflection of the top surface provides the gravitational load required for $v = 0$ (e.g. McKenzie, 1977). For the horizontal component we consider both a free-slip (for which tangential stress, $\sigma_{rz} = 0$) and a rigid upper boundary (both velocity components $u = v = 0$). Both types of condition may be relevant, and the upper surface boundary condition clearly can influence the style and amplitude of dynamic topography (Zhong et al., 1996).

To simplify the application of boundary conditions at the base of the lithosphere, a reference column of density ρ_a is subtracted from the system, so that the effective density of the asthenosphere is zero, that of the crust is $\rho_c - \rho_a$, that of the atmosphere above the crust is $-\rho_a$, and that of the lithosphere is $\Delta\rho = \rho_m - \rho_a$. The asthenosphere is assumed to be relatively inviscid, so that the base of the lithosphere (initially at $z = -h$) may be treated as a stress-free surface (both components of traction are zero). On the boundary between crust and mantle layers (initially at $z = -m$), both velocity and traction are continuous. On the central axis ($r = 0$), $u = 0$ and $\sigma_{rz} = 0$ are required for conservation of mass and momentum. We assume the same conditions apply at radius $r = R_0$, representing a free-slip perimeter, analogous to the reflecting condition often used in 2D plane-strain calculations.

At time zero, the initially flat interface at the base of the lithosphere is displaced vertically by a small perturbation ($\pm 1\%$) that could be attributed to variation in basal heat-flow or stress induced by convection in the layer beneath the lithosphere. An arbitrary radial variation in this deflection function can be described using combinations of the Bessel functions $J_0(kr)$ and $J_1(kr)$ with an appropriate combination of wavenumbers. The function $J_0(kr)$ has a maximum at $r = 0$, as required for generation of an instability with either central upwelling ($+$) or central downwelling ($-$). In representing cases of central downwelling we vary R_0 and select k so that $kR_0 = 3.8317$ (the first zero), representing a half wavelength. For central upwelling cases, we chose k so that $kR_0 = 7.0156$ (the second zero), representing a full wavelength. In order to compare the two cases at the same wavenumber, R_0 is greater by the factor $7.0156/3.8317$ for central upwelling than for central downwelling experiments.

The governing equations are rendered dimensionless using length scale h, density scale $\Delta\rho$, and stress scale $gh\Delta\rho$. The natural time scale for viscous flow is then

$$t_0 = \frac{2\eta_m}{gh\Delta\rho}. \tag{7}$$

Key non-dimensional parameters (indicated with a prime) that govern the solutions then are the relative crust/mantle density ratio

$$\rho_c' = \frac{\rho_c - \rho_a}{\Delta\rho}, \tag{8}$$

the crust/mantle viscosity ratio

$$\eta_c' = \frac{\eta_c}{\eta_m} \tag{9}$$

and the crust/lithosphere thickness ratio

$$m' = \frac{m}{h}. \tag{10}$$

Assuming densities for mantle ($\rho_m = 3330 \text{ kg m}^{-3}$) and asthenosphere ($\rho_a = 3300 \text{ kg m}^{-3}$), similar to terrestrial values, and attributing the difference in density between lithosphere and asthenosphere to thermal expansion ($\Delta\rho = \rho_a\alpha\Delta T$, with thermal expansion coefficient, α of $3 \times 10^{-5} \text{ K}^{-1}$, $\rho_a = 3300 \text{ kg m}^{-3}$, and average temperature difference $\Delta T = 360 \text{ K}$), we estimate $\Delta\rho = 30 \text{ kg m}^{-3}$ (subject to unknown compositional variation). Assuming crustal density of $\sim 2800 \text{ kg m}^{-3}$, we therefore use $\rho_c' = -16.7$ in all of the numerical experiments described here. With crustal thickness estimates obtained from analysis of gravity and topography typically in the range 10–60 km in coronae regions (e.g. Grimm and Hess, 1997; Hoogenboom et al., 2004), and lithospheric thicknesses between 40 and 100 km (Kaula and Phillips, 1981; Phillips and Malin, 1983; Phillips, 1990; Solomon and Head, 1982), we consider values of $m' = 1/6$, $1/3$, and $1/2$. Topography and gravity anomalies in the following diagrams are presented for $g = 10 \text{ m s}^{-2}$, $h = 100$ km and $\Delta\rho = 30 \text{ kg m}^{-3}$. The relative crustal viscosity parameter η_c' is poorly constrained and we consider values in the range 0.05–25. The absolute viscosity scale η_m is likewise poorly constrained, and therefore we retain a dimensionless timescale in results presented below.

2.3. Surface topography and gravity

To calculate topographic variation on the upper surface, variations in vertical normal stress are assumed to be in static equilibrium with the topographic burden of assumed density ρ_c and amplitude $H(r)$:

$$H = h\frac{\Delta\rho}{\rho_c}\sigma_{zz}' = h\frac{\Delta\rho}{\rho_c}\left(p' + 2\eta'\frac{\partial v'}{\partial z'}\right), \tag{11}$$

where σ_{zz}' is dimensionless normal stress evaluated at $z = 0$, h is the lithospheric thickness and $\Delta\rho$ is the density difference between the lithosphere and the asthenosphere. The density of the atmosphere is assumed negligible relative to ρ_c.

The vertical component of the gravity anomaly at (r_0, z_0) is calculated using a surface integral around each constant density region. The integral in the θ direction (around the axis of symmetry) may be expressed as the complete Legendre elliptic integral of the first kind $F(\pi/2, k)$:

$$\Delta g = -4G\Delta\rho \oint_{\partial\Omega}\left(\frac{rF(\pi/2, \kappa(r, z))}{a(r, z)}\right)dr, \tag{12}$$

where $a(r, z) = \sqrt{(r + r_0)^2 + (z_0 - z)^2}$, $\kappa(r, z) = 2\sqrt{rr_0}/$ $a(r, z)$, (r_0, z_0) is the measurement point, and (r, z) are the co-ordinates of the path in the vertical plane around each constant density region. Gravity is also influenced by material outside the solution domain. For the purpose of the gravity calculation, the layer is assumed to continue to infinite radius, stratified as at $r = R_0$. For this reason, solutions were avoided in which downwelling of the layer occurred at $r = R_0$.

Equation (12) is applied once for the crust-mantle inter-face (density contrast $\rho_c - \Delta\rho$) and once for the lithosphere–asthenosphere interface (density contrast $\Delta\rho$) to compute the Bouguer anomaly. To calculate the free-air anomaly, the effect of mass in the topography above $z = 0$ is also included by a further application of Eq. (12) to the topography function $H(r)$ (density contrast $-\rho_c$). Model calculations here assume a mea-surement height for gravity of 5000 m above the reference level.

3. Results

3.1. Growth-rate and wavenumber

When the perturbation is a small pure harmonic disturbance (i.e. a simple multiple of the Bessel function $J_0(kr)$), the gen-eral analytic solution consists of two terms that grow or decay exponentially (Neil and Houseman, 1999; Molnar and House-man, 2004). The growing term is driven by the unstable stratifi-cation at the base of the model lithosphere, while the decaying term is driven by the stable stratification at the base of the crust. The dimensionless growth-rate $q'(k') = t_0 q(hk)$ of the unsta-ble term determines the timescale over which the instability grows. If a range of wavenumbers is present in the initial per-turbation (e.g. if developed from a random perturbation), the wavenumber for which q' is a maximum soon dominates the so-lution. For the numerical experiments shown, we investigated a range of wavenumbers in order to approximately identify the maximum growth-rate of the instability. We used eight dif-ferent dimensionless wavenumbers: $k' = kh = 20.94$, 12.56, 6.28, 4.19, 2.09, 1.39, 1.05, 0.52 (corresponding to domain radii $R_0/h = 0.3$, 0.5, 1.0, 1.5, 3, 4.5, 6, and 12, for central downwelling, and the same set multiplied by 1.8309 for central upwelling).

The growth-rate of the instability is determined from the gra-dient of the graph of the natural log of the maximum displace-ment versus dimensionless time. Central downwelling models theoretically grow at the same rate as central upwelling mod-els in the early stage of growth. If the deformation is small, the numerically determined linear growth-rates agree within 3% for the two forms of the instability. For $m' = 0$ and free-slip upper boundary, growth-rate increases monotonically with wavelength, and is maximum ($q' = 0.5$) for $k' = 0$. For rigid up-per boundary, growth rates peak at wavelengths comparable to the layer thickness ($k < \sim 2.5$) and decay to zero at long wave-lengths. At short wavelengths, growth rates are similar for both conditions.

The growth-rates for $m' = 0$ are, within numerical uncer-tainty, the same as those obtained by Conrad and Molnar (1997) for 2D plane-strain instability. While the perturbation is small

the dependences on parameters m', η_c', and ρ_c' of growth-rates $q'(k')$ (previously described by Neil and Houseman, 1999), ap-ply equally to the axisymmetric problem. The axisymmetric problem differs essentially from the plane-strain problem in the asymmetry between peripheral upwelling and central down-welling (or vice versa), and the consequences of this asymmetry for the development of the instability into the large amplitude domain.

3.2. Instability without crustal layer

Growth of the R–T instability for a central downwelling ex-periment is compared with that of a central upwelling experi-ment in Fig. 3 for the case of a uniform mantle layer without a crust. Central downwelling (Fig. 3a) occurs for a positive ini-tial perturbation in lithospheric thickness on the axis ($r = 0$), central upwelling (Fig. 3b) for a negative perturbation. In this illustration a relatively long wavelength is assumed, consistent with the highest growth rates occurring for zero wavenumber.

Thickening of lithosphere pulls the surface downwards, cre-ating a topographic basin over the downwelling, whose depth increases with time (Fig. 3c). For central upwelling models with a free-slip upper boundary, a rise develops over the axis of symmetry (Fig. 3d), caused by lithospheric thinning beneath the centre. A much deeper trough is created over the annular re-gion of downwelling. At this wavenumber the downwelling drip shifts slightly towards the centre of axisymmetry as it grows, which causes the sides of the trough to become steeper, and the central dome more plateau-like, with time (Fig. 3d, $t' > 0.85$).

The free-air gravity profiles (Figs. 3e and 3f) are qualita-tively similar in shape and sign to the topography profiles. Negative free-air gravity anomalies are calculated over the depressed topography whether downwelling is central or pe-ripheral, but significant positive highs develop on the sides of the negative trough in Fig. 3f. Gravity anomaly amplitudes may be somewhat greater for the central upwelling experiment (Fig. 3f) when compared to the central downwelling experiment (Fig. 3e) at a comparable stage of growth.

3.3. Effect of a low-density crustal layer

We next consider a model lithosphere that includes a crustal layer with initial crust to lithosphere thickness ratio of $m' = 1/6$, and no viscosity contrast between the crust and mantle ($\eta_c' = 1$). The deflection of the base of the lithosphere as the instability develops is shown for central downwelling (Fig. 4a) and central upwelling (Fig. 4b). Also shown (as dashed lines), are the depths of the crust–lithosphere boundary at the begin-ning (flat line) and at the last time step. Compared with the no-crust models, the low-density crustal layer reduces the growth-rate q' and decreases the wavelength of maximum growth, because the buoyant crustal layer inhibits the growth of the in-stability.

In both experiments crustal thickening occurs over the down-welling. The asymmetry between central downwelling and cen-tral upwelling is clearly evident in the final crustal thickness
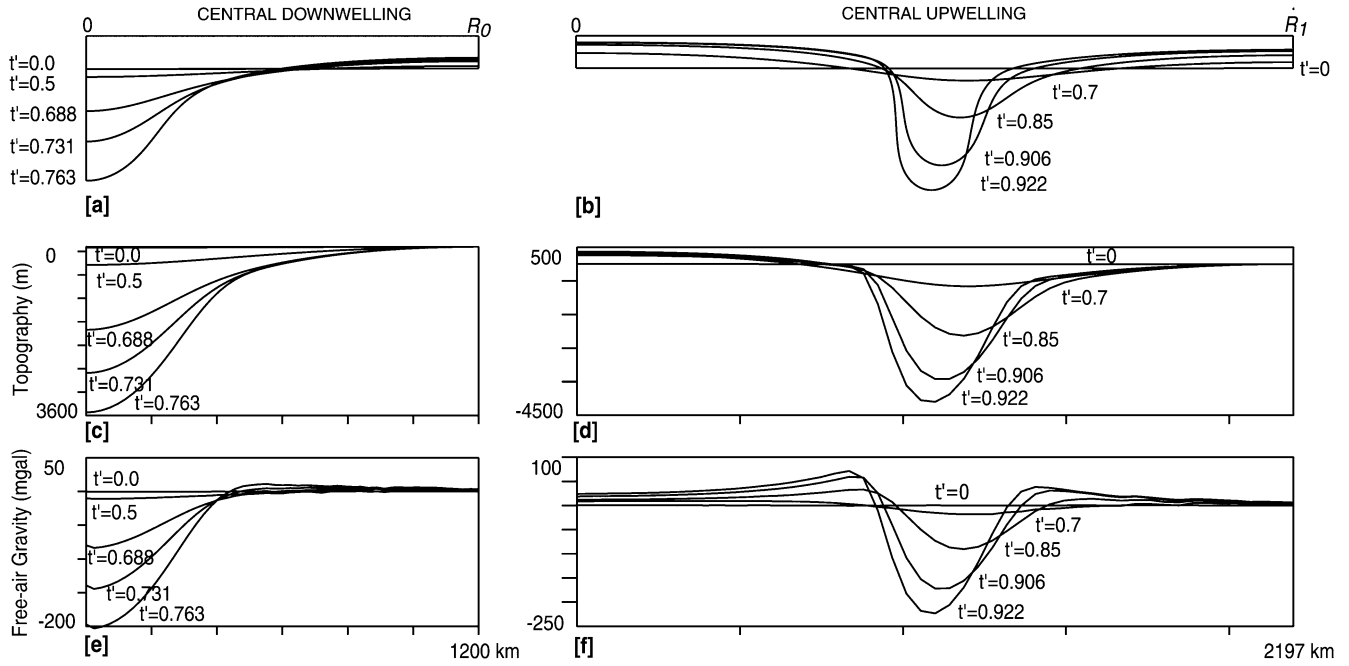
Fig. 3. Lithosphere–asthenosphere boundary (a,b), topography profiles (c,d), and gravity anomaly profiles (e,f), at five successive dimensionless times during the growth of the Rayleigh–Taylor instability, for the case of central downwelling (a,c,e) and central upwelling (b,d,f), in cylindrical axisymmetry with $\eta'_c = 1$, $m' = 0$, $k' = 0.3193$ ($R_0 = 12$ and 21.97 for (a) and (b), respectively), and free-slip upper surface. Topography (c, d) is arbitrarily zeroed at $r = R_0$. Gravity (e,f) approaches zero as $r \to \infty$, assuming that the structure at $r = R_0$ extends uniformly to infinity.
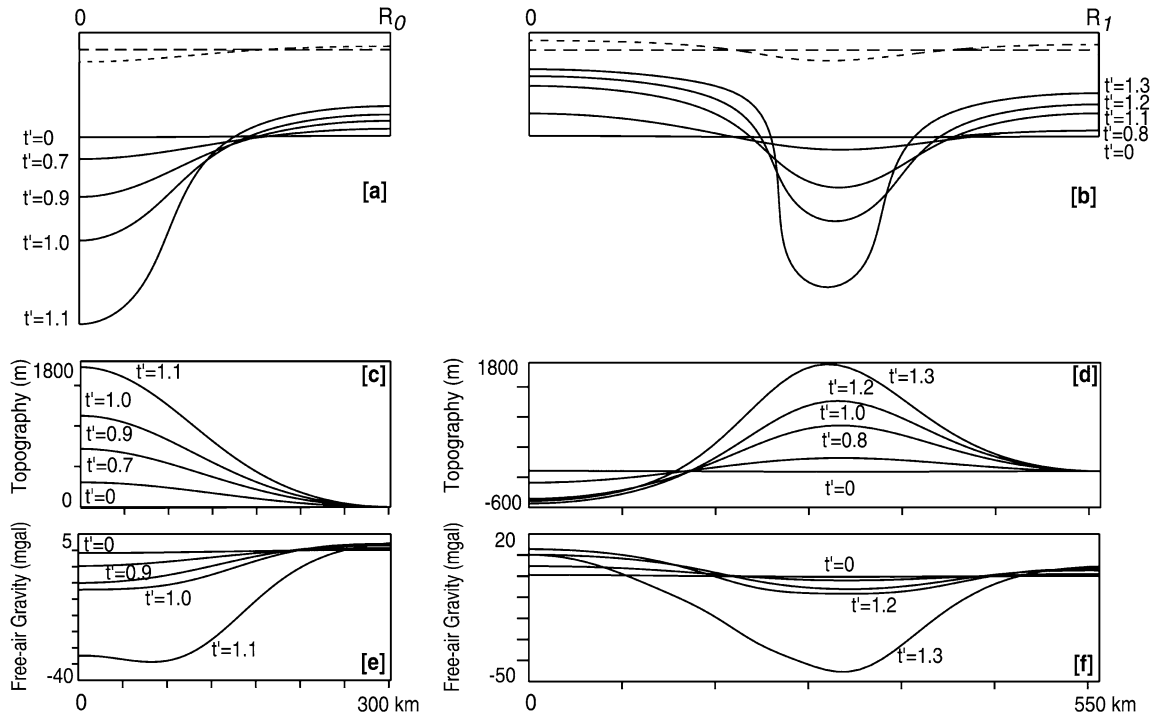

Fig. 4. Lithosphere–asthenosphere boundary (a,b), topography profiles (c,d), and gravity anomaly profiles (e,f), at five successive dimensionless times during the growth of the Rayleigh–Taylor instability, for the case of central downwelling (a,c,e) and central upwelling (b,d,f), in cylindrical axisymmetry with $\eta'_c = 1$, $m' = 1/6$, $\rho'_c = -16.7$, $k' = 1.2772$ ($R_0 = 3$ and 5.49 for (a) and (b), respectively), and free-slip upper surface. Dashed lines near the top of (a) and (b) denote the depths of the crust–lithosphere boundary at the beginning and end of the experiments. Other conventions are as for Fig. 3.

distributions of these two experiments. With central downwelling (Fig. 4a) peripheral crustal extension is relatively modest. For the central upwelling experiment (Fig. 4b), however,

major lithospheric extension occurs beneath the central zone, with downwelling and crustal shortening in the surrounding annular region. Mantle flowing downward in the annular region is

replaced by lower-density asthenosphere that moves up in the centre as part of the convective overturn. The crust is thickened above the downwelling (by a factor of ∼1.6) and thinned in the central region (by a factor of ∼2.2) at the end of the experiment.

The buoyancy of the thickened crust over the downwelling causes the surface to rise in these regions (Figs. 4c and 4d). For central downwelling, continued thickening in the centre pushes the surface upwards, creating a dome, which grows with time (Fig. 4c). For central upwelling the high topography forms an annular ridge of comparable height surrounding a low central topographic depression (Fig. 4d). Compared to Fig. 3, the signs of the topography anomalies over the downwellings are reversed. With the crust present, topography has isostatic (related to crustal thickness variation) and dynamic components. Crustal thickening clearly may cause positive topography that is greater than the negative dynamic topography (Figs. 4c and 4d).

The free-air gravity anomaly is more difficult to analyse since it includes a positive component from the dense lithospheric root, a negative component from the dynamic topography, a negative component from the crustal root, and a positive component from the isostatic component of topography. In general the topographic contributions outweigh those caused by the density anomalies at depth, but whether the isostatic component outweighs the dynamic component depends on the extent of crustal deformation. In Figs. 4e and 4f the negative components of the free-air gravity signal dominate over the downwellings, though they are smaller in amplitude than those of Figs. 3e and 3f by a factor of ⩾5. Similar trends are also observed in the topography and gravity anomalies calculated for models with a rigid upper boundary, although the amplitudes of both topography and gravity are reduced compared to those obtained with free-slip experiments.

3.4. Influence of crustal viscosity ratio η_c'

In the next set of experiments we varied the ratio of crustal to lithospheric viscosity (η_c') between 0.05 and 25. In these calculations, we assume a layer thickness of $m' = 1/6$. To illustrate the effect of crustal viscosity on topography and gravity, two end-member experiments are described: $\eta_c' = 25$ (Fig. 5), and $\eta_c' = 0.05$ (Fig. 6). In each case we chose a wavenumber near that of maximum growth rate. The wavenumber of maximum growth rate is reduced for the strong crust, because the base of the crust behaves like a rigid upper boundary resisting horizontal movement. In contrast longer wavelengths grow faster for the weak crust because of the reduced resistance to horizontal movement.

In general, if the viscosity of the upper layer is much greater than that of the lower layer, the thickness of the crust stays approximately the same, regardless of upper boundary condition or wavenumber (e.g. Fig. 5). However the crust transmits the stress created by the mantle downwelling that pulls the surface downward into a topographic depression, growing deeper with time (Figs. 5c and 5d). With negligible contributions from crustal thickness variation, the free-air gravity anomaly is dominated by the depression of the upper surface to produce a

negative anomaly above the downwelling lithosphere whose amplitude also increases with time (Figs. 5e and 5f).

Although the crust undergoes little thinning in the central upwelling experiment (Fig. 5b) the lithosphere in the central region is thinned by a factor of between 2 and 3 at the end of the experiment, creating a huge contrast in lithospheric thickness compared to the surrounding annular region. As the lithosphere is pushed upwards and thinned over the central upwelling, the topography is also pushed upwards into a dome surrounded by a trough over the annular downwelling (Fig. 5d). The dome increases in height with time, eventually assuming a plateau-like profile. Because the variations in crustal thickness are so small in these experiments, the free-air gravity anomaly profiles have a similar shape to the topographic profiles (Fig. 5f). Comparable experiments with a rigid upper boundary show similar topographic and gravity anomaly profiles.

If the crust is 20 times weaker than the mantle ($\eta_c' = 0.05$) the crust is easily deformed, and in the course of the experiment is thickened by almost a factor of 2 over the central downwelling (Fig. 6a). The topographic profile over the central downwelling (Fig. 6c) becomes dome-shaped as the uplift associated with the progressively thickening crust overwhelms the dynamic component of subsidence caused by mantle downwelling. The free-air gravity anomaly, however, continues to be dominated by the negative contribution to the topographic signal from dynamic stress, and the broad negative anomaly increases in amplitude with increasing time (Fig. 6e). Compared to the experiment with no variation in viscosity between the crust and mantle (Fig. 4), we see firstly that the shapes of gravity and topography profiles are similar, and secondly that the low crustal viscosity reduces the amplitude of topography by perhaps 1/3, whereas the amplitude of the gravity anomaly is increased by about a factor of two. Similar topography and gravity profiles are observed in the corresponding experiments with a rigid upper boundary except that the height of the topography is reduced by as much as a factor of 1.3 at comparable stages of development of the instability.

3.5. Influence of crustal thickness ratio m'

The relationship between growth-rate and wavenumber is shown in Fig. 7 for values of $m' = 1/3$, $1/2$, $1/6$ and 0, for both free-slip and rigid upper boundaries. As m' increases and the crust is a greater percentage of the combined layer thickness, the growth-rate q' decreases for either upper boundary condition, though the effect is small for wavenumbers greater than ∼6. Differences between free-slip and rigid upper boundary experiments are most apparent at small wavenumbers with m' less than ∼1/3 (compare Figs. 7a and 7b). The crust is limited in its ability to deform and its buoyancy resists thickening with either boundary condition (Neil and Houseman, 1999). Thinner crust is less able to mask the effect of the upper boundary and, for a free-slip boundary, the growth rate is observed to increase significantly at small wavenumber as the crust is thinned (Fig. 7a).

To illustrate the effect of a relatively thick crust (or thin lithosphere), on topography and free-air gravity, Fig. 8 shows

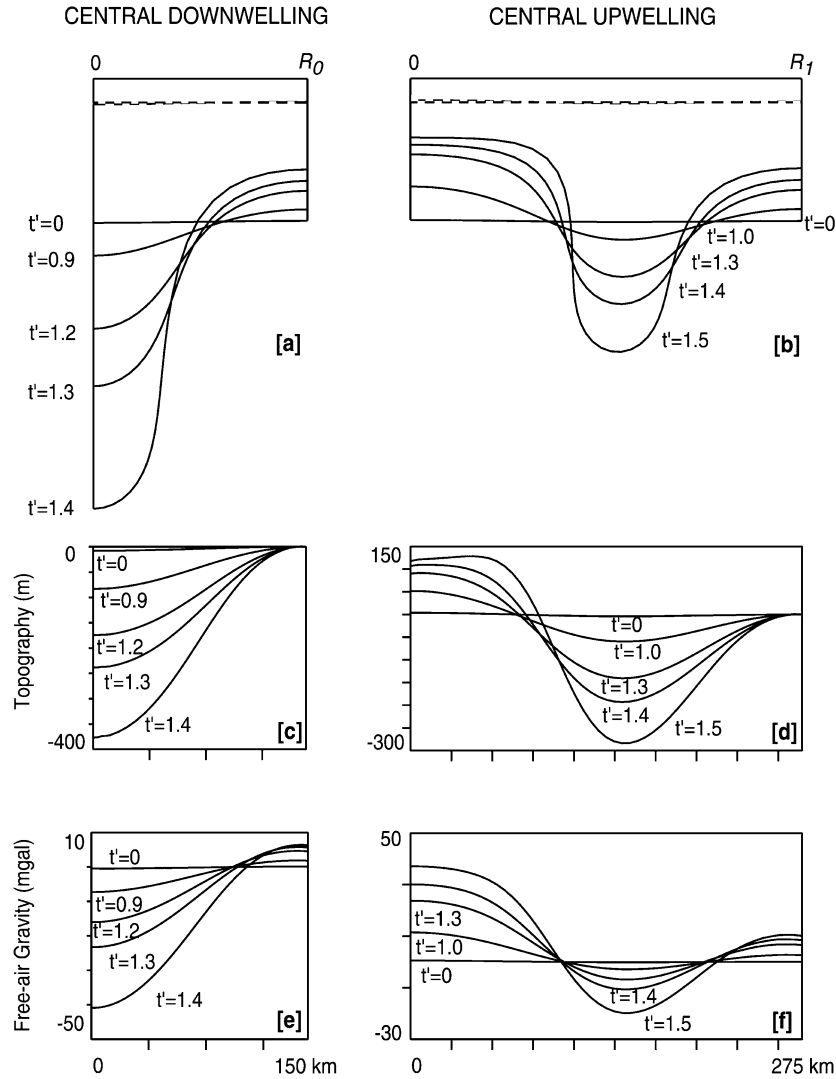CENTRAL DOWNWELLING   CENTRAL UPWELLING

Fig. 5. Lithosphere–asthenosphere boundary (a,b), topography profiles (c,d), and gravity anomaly profiles (e,f), at five successive dimensionless times during the growth of the Rayleigh–Taylor instability, for the case of central downwelling (a,c,e) and central upwelling (b,d,f), in cylindrical axisymmetry with $\eta'_c = 25$, $m' = 1/6$, $\rho'_c = -16.7$, $k' = 2.554$ ($R_0 = 1.5$ and 2.75 for (a) and (b), respectively), and free-slip upper surface. Other conventions are as for Fig. 4.

central upwelling and central downwelling experiments for $m' = 1/2$ with crust that is relatively weak ($\eta'_c = 0.25$). With central downwelling, the crust thickens by a factor of ~1.1 over the downwelling (Fig. 8a). As for Fig. 6a, the topography is briefly depressed over the downwelling then becomes dome-shaped as the uplift associated with the thickening crust exceeds the dynamic component of subsidence related to the mantle downwelling (Figs. 8c and 8d). The topographic relief is much less than that predicted for a thinner crust, whether the crust is weaker (e.g. Figs. 6c and 6d) or somewhat stronger (e.g. Figs. 4c and 4d). Therefore the free-air gravity anomalies (Figs. 8e and 8f) remain negative over the downwellings, and their amplitudes comparable to those of thinner stronger crust (Fig. 4).

For the corresponding experiment with central upwelling ($\eta'_c = 0.25$, $m' = 1/2$), crustal thickening by a similar factor (~1.13) occurs above the downwelling (Fig. 8b). The most noteworthy aspect of this experiment, however, is the extreme

degree of lithospheric thinning in the central region, even though crustal thickness is almost unaffected. Lithospheric thinning causes uplift, resulting in a central plateau that is surrounded by an annular ridge caused by crustal thickening above the downwelling (Fig. 8d). The same experiments with a rigid upper boundary show comparable development of the lithospheric downwelling but reduced degree of crustal thickening.

4. Discussion

A successful model of coronae formation should explain the wide variety of observed shapes, diameters, topographic profile heights, free-air gravity anomalies (Table 1) and presence or absence of volcanism and extensional or convergent structures at the surface. Although mantle upwellings are the favoured mechanism for the formation of hot-spot rises, lithospheric gravitational instabilities may develop independently of plumes that have originated deep within the mantle.
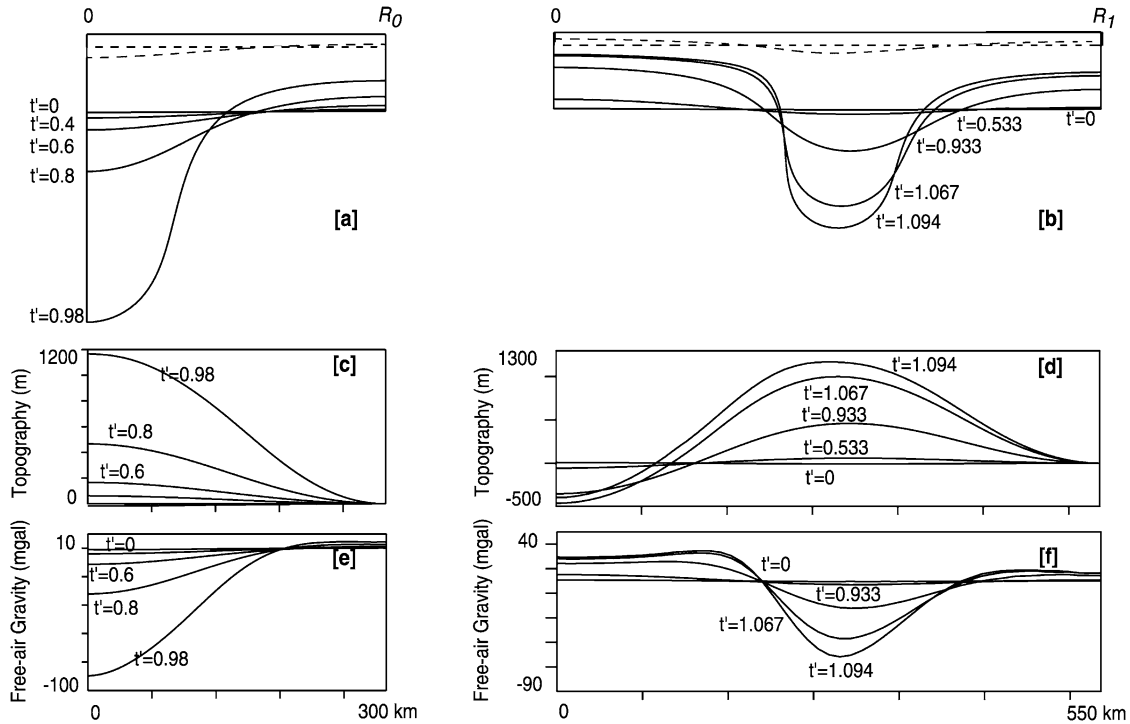
Fig. 6. Lithosphere–asthenosphere boundary (a,b), topography profiles (c,d), and gravity anomaly profiles (e,f), at five successive dimensionless times during the growth of the Rayleigh–Taylor instability, for the case of central downwelling (a,c,e) and central upwelling (b, d, f), in cylindrical axisymmetry with $\eta'_c = 0.05$, $m' = 1/6$, $\rho'_c = -16.7$, $k' = 1.277$ ($R_0 = 3.0$ and 5.49 for (a) and (b), respectively), and free-slip upper surface. Other conventions are as for Fig. 4.
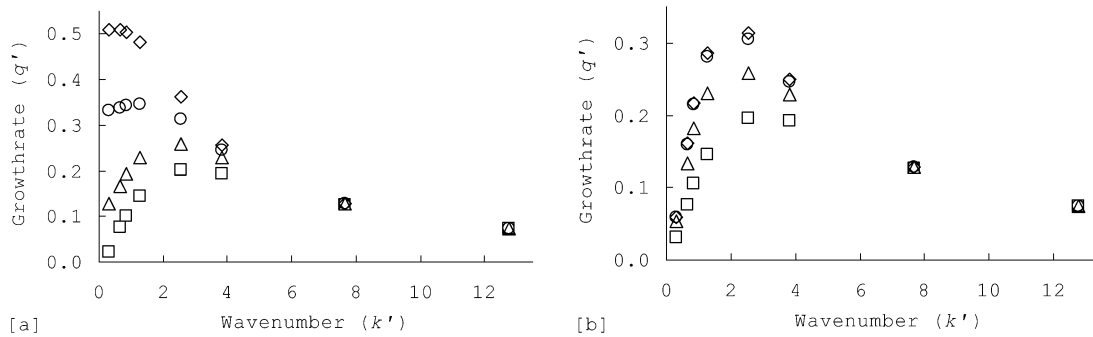

Fig. 7. Dimensionless growth-rate (measured from numerical experiments) versus dimensionless wavenumber, for axisymmetric Rayleigh–Taylor instability for (a) free-slip and (b) rigid upper boundary, each with $\eta'_c = 1$ and $\rho'_c = -16.7$. Diamonds represent $m' = 0$; circles, $m' = 1/6$; triangles, $m' = 1/3$; and squares, $m' = 1/2$.

In interpreting our model profiles, we note several simplifications necessary to obtain practical solutions: Firstly, the instability would continue to evolve after our calculations stop (limited by mesh distortion). Detachment of the downwelling material and subsequent gravitational relaxation of the base of the crust and upper surface would probably then occur, accompanied by a decrease in amplitude of gravity and topography anomalies. The ratio of gravity to topography anomaly for such a relict corona should be preserved even though the peak amplitudes would presumably be much reduced with further elapsed time. Secondly, the truncation of the model at $r = R_0$ may introduce a bias in the inferred background levels for elevation and gravity. We have also omitted erosion, brittle failure of the crust and the elastic response of the lithosphere. While the elastic response of the lithosphere will act to redistribute surface deflection at short wavelengths, leading to broader topography

(Turcotte and Schubert, 2002), the wavelengths of these structures may well be great enough that the flexural effect is small. Erosion is not expected to play a major part in the deformation of corona structures given the low rates of erosion inferred on Venus (Arvidson et al., 1992). We also omit the effects of non-Newtonian viscosity, which may require a large initial perturbation to overcome the stabilising effect of thermal diffusion (Houseman and Molnar, 2001), and assume that the viscosity of the underlying asthenosphere is negligible, which is accurate if its viscosity is less by a factor of 10 or more than that of the mantle (Conrad and Molnar, 1997). Conduction of heat, and the thermal subsidence that would result from lithospheric extension and thermal re-equilibration (e.g. McKenzie, 1977), are also omitted; we assume that the instability is fast compared to thermal re-equilibration.
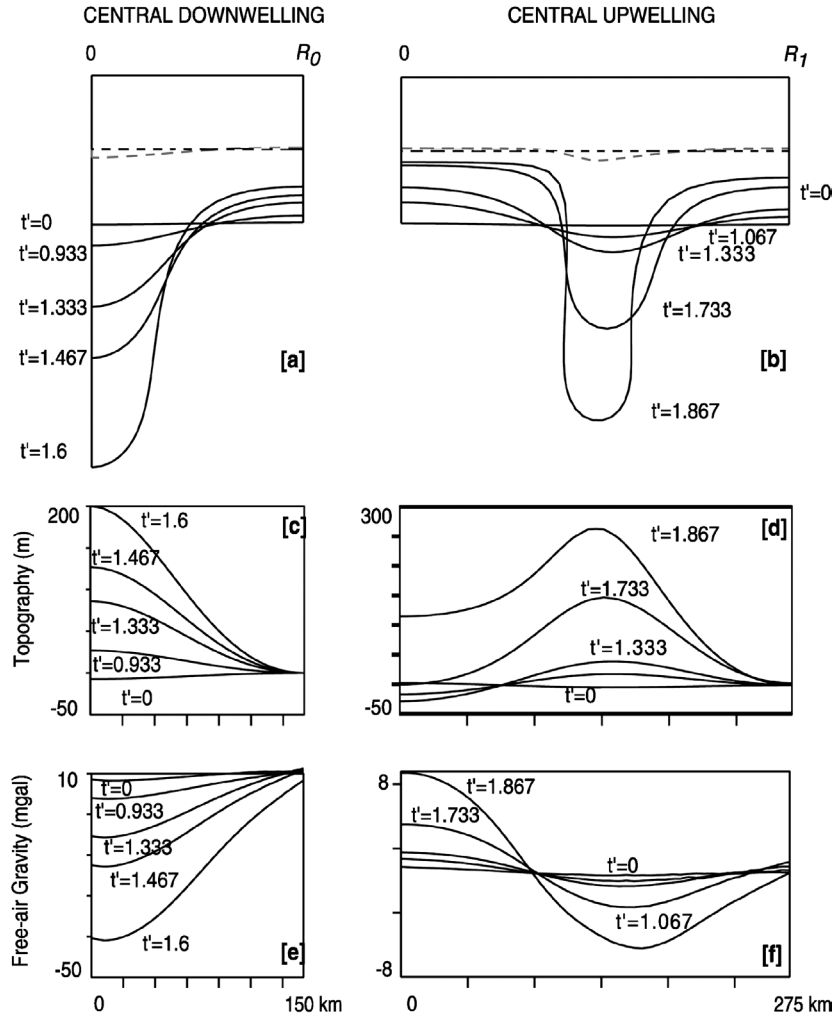
Fig. 8. Lithosphere–asthenosphere boundary (a,b), topography profiles (c,d), and gravity anomaly profiles (e,f), at five successive dimensionless times during the growth of the Rayleigh–Taylor instability, for the case of central downwelling (a,c,e) and central upwelling (b,d,f), in cylindrical axisymmetry with $\eta_c' = 0.25$, $\rho_c' = -16.7$, $m' = 1/2$, $k' = 2.554$ ($R_0 = 1.5$ and 2.75 for (a) and (b), respectively), and free-slip upper surface. Other conventions are as for Fig. 4.

In what follows, we systematically compare observational measurements from venusian coronae, with the predictions of these models in order to infer constraints on the thickness and effective viscosity of the venusian lithosphere.

4.1. Topographic shape

Coronae topographic profiles have been classified into nine groups (Table 1) by Smrekar and Stofan (1997). Most of the standard profile types can be explained by the gravitational instability model, although some are better explained by central upwelling and some by central downwelling (Table 1).

Within the parameter space examined, examples of simple depressions (Group 8) are provided by experiments in which there is no crustal layer (e.g. Fig. 3c) or in which the crustal layer has a high viscosity (e.g. Fig. 5c). Domes (Group 1) are provided by experiments with a low-density crustal layer and central downwelling (e.g. Figs. 4c, 6c, 8c). Central downwelling initially induces a small depression that, depending on the viscosity of the crust, evolves into either a dome or a deeper depression, with time. High-viscosity crust is flexed downward

above a mantle downwelling, whereas crust whose viscosity is less than or similar to that of the mantle shortens horizontally, thickens and forms a dome at the surface. Domes or plateaus surrounded by a trough are also predicted in some cases of central upwelling if the crust is very viscous (Fig. 5d) or absent (Fig. 3d).

Topographic groups 2, 3, 4, and 7 (Table 1) are better explained by models that are driven by central upwelling, with variations in topographic profile depending on the initial crust/lithosphere thickness ratio m', viscosity of the crust η_c', and time t. However, it is possible that plateaus evolve from domes by gravitational spreading that follows the initial instability. If the crust is sufficiently thick or weak (e.g. Fig. 8d), topography evolves from rim surrounding depression (Group 4), to rim-only (Group 7), and eventually to rim surrounding interior high (Group 3a). The evolution of rim-only coronae (Group 7) from rimmed-depression coronae (Group 4) is also predicted for models of coronae formation based on upwelling diapirs (Koch and Manga, 1996) or plumes (Smrekar and Stofan, 1997).

Table 1
Observed coronae properties

Group	Topographic profile	Description (# of coronae)	Observed diameter (km)			Observed peak free-air gravity (mgal)			Observed peak topographic deflection (m)			GTR (mgal km^{-1})		
			Min. max.	Med.	Ave. std. dev.	Min. max.	Med.	Ave.(#) std. dev.	Min. max.	Med.	Ave. std. dev.	Min. max.	Med.	Ave. std. dev.
1		Dome (30)	75 552	150	201 109	−68 128	41	28(10) 67	300 3300	1533	1667 921	−153 43	22	−4 60
2		Plateau (52)	60 850	292	306 160	−75 142	49	40(23) 55	400 3500	1700	1826 989	−38 106	36	27 33
3a		Rim surrounding interior high (39)	145 630	300	327 119	10 198	51	64(23) 45	600 2300	1250	1267 477	8 88	52	46 23
3b		Rim surrounding interior dome (64)	91 810	288	309 146	−50 93	13	18(22) 44	100 2300	650	783 578	−125 125	3	−11 75
4		Rim surrounding depression (111)	64 1155	170	195 135	−79 72	−35	−23(21) 45	−2600 −120	−810	−930 679	−283 153	−33	−36 89
5		Outer rise, trough, rim, inner high (22)	118 600	313	341 145	– –	–	– –	– –	–	– –	– –	–	– –
6		Outer rise, trough, rim, inner low (6)	150 2600	207	622 973	– –	–	– –	– –	–	– –	– –	–	– –
7		Rim only (31)	120 1060	200	269 186	−65 47	0	−1(5) 39	200 1300	600	760 513	−50 78	−38	−10 56
8		Depression (39)	60 450	145	166 87	−62 −10	−33	−35(8) 18	−3800 −400	−1100	−1300 1120	9 90	35	38 26
9		No discernible signature (13)	60 330	150	166 75	– –	–	– –	– –	–	– –	– –	–	– –

Topographic Groups are defined (Smrekar and Stofan, 1997), including the total number of coronae observed in each group (parentheses). Diameter is calculated as the outermost extent of the concentric deformation (Stofan et al., 1992). Peak free-air gravity anomalies were measured for a subset of 112 coronae for which the gravity field is locally resolved (Johnson and Richards, 2003). Subscripts indicate the number of coronae sampled in each group. Peak topographic deflections away from the background level were calculated for the same 112 coronae over the centre of each corona (with the exception of Groups 3a and 7 where the peak topography was measured over the rims). Peak gravity/topography (GTR) ratio is calculated by dividing the peak free-air gravity anomaly by the peak topographic deflection. The minimum, maximum, median, average and standard deviation for each group measurement is also provided. Data for Groups 5 and 6 (comprising 6% of the corona population) are omitted from this table for lack of adequately resolved gravity data in the relevant regions.

More complex topography (e.g. Group 3b) is found with central upwelling models in a few instances where a secondary instability with shorter wavelength develops after the initial central upwelling (e.g. Fig. 9, with $\eta'_c = 0.05$, $m' = 1/2$). Additional peripheral ridges and troughs are observed with Group 5 and 6 coronae (defined by outer rise, trough, rim, and inner high or low) and may be predicted if higher Bessel modes are permitted to grow, as occurs in Fig. 9.

4.2. Coronae diameters

For a model lithospheric thickness of $h = 100$ km, domes (e.g. Figs. 4c, 6c, 8c) and depressions (e.g. Fig. 5c) have scaled diameters ($2R_0$) of 300–600 km (depending on k', η', and m'). Thus the range of model diameters is consistent with the observed average diameter of 200 km for domes and depressions (Table 1), if the nominal value of the scaling parameter h is reduced by approximately 1/2, to $h = 50$ km (with uncertainty

of a factor of ~2). Thinner lithosphere does not, however, exclude the possibility of larger coronae developing in response to small wavenumber disturbances.

The other topographic groups (plateaus, rimmed plateaus, domes with surrounding rims, and rim only) whose profile types are better explained by a central-upwelling model (see previous section) have observed average diameters of ~300 km (Table 1; Stofan et al., 1992). With $h = 100$ km, the examples shown in Figs. 4d, 5d, 6d, 8d, and 9b have model diameters in the range 500–1000 km. Because the model diameter scales directly with h, the observed average diameter of 300 km for these topographic groups, again implies lithospheric thickness $h = 50$ km, with uncertainty of a factor of ~2. Such values of h, smaller than expected, explain the average group diameters, but we note that there is great variability in the data, and numerous examples of large coronae whose diameter is more consistent with a thicker lithosphere, or at least longer wavelength disturbances.
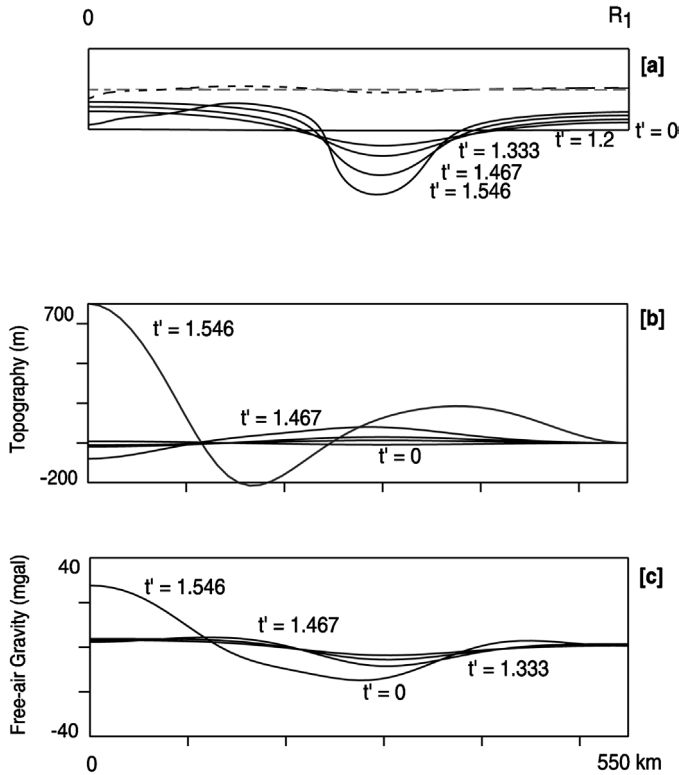
Fig. 9. Lithosphere–asthenosphere boundary (a), topography profiles (b), and gravity anomaly profiles (c), at five successive dimensionless times for an experiment begun with central upwelling in cylindrical axisymmetry, $\eta'_c = 0.05$, $\rho'_c = -16.7$, $m' = 1/2$, $k' = 1.277$ ($R_0 = 5.49$), and free-slip upper surface. The dashed lines in (a) show the boundaries between the crust and lithosphere at beginning and end of the experiment.

4.3. Amplitude of topography

Observations of peak coronae topographic heights (Table 1) provide further constraints on model parameters. Topographic amplitudes typically are on the order of 1000 m, but vary from effectively zero (within measurement error of ~100 m (Pettengill et al., 1991)) to ~3000 m.

For a range of experiments we calculated the amplitude of model topography (e.g. Figs. 3c–3d, 4c–4d, 5c–5d, 6c–6d, 8c–8d, 9b), assuming values within the expected ranges of parameters ρ'_c, m', and η'_c, and nominal dimensionalisation constants $h = 100$ km and $\Delta\rho = 30$ kg m^{-3} (Eq. (11)). The scaling parameters are not unique: the same topographic scale results if we reduce h to 60 km and increase $\Delta\rho$ to 50 kg m^{-3}. The model topographic heights fall within the observed range of topographic heights however, suggesting that $h\Delta\rho = 3 \times 10^6$ kg m^{-2} is (within a factor of 2 or so) the correct value to use in scaling our experiments. Some combinations of m' and η'_c (e.g. Figs. 8c and 8d) do not give rise to topographic amplitude on the kilometre scale without a significantly greater value of $h\Delta\rho$. In those cases the dynamic component of topography has comparable magnitude and opposite sign to the component caused by crustal thickening. In other cases, one of these components dominates, and we easily predict kilometre-scale topography. This variability in model amplitudes appears to be reflected in the data variability (Table 1). It is therefore

difficult to use the amplitude of topography alone to better constrain the key physical and non-dimensional parameters.

For the scaling factors $h\Delta\rho \sim 3 \times 10^6$ kg m^{-2} and $h = 50$ km (from analysis of coronae diameters) we infer $\Delta\rho \sim 60$ kg m^{-3}. If this density excess is explained by thermal contraction, it implies a mean temperature contrast between lithospheric mantle and convection layer of about 600 K (all of these numbers uncertain within about a factor of 2). The mean temperature contrast, however, is expected to be at most about 475 K. Explanation of the density anomalies in terms of thermal expansion is therefore possible, but we acknowledge that density differences caused by compositional variation present possible alternative mechanisms.

4.4. Free-air gravity anomalies

Gravity data were obtained from Magellan over 98% of Venus, at altitudes of 155–220 km. These data have been downward continued to the surface, and analysed to determine a new spherical harmonic representation of the gravity field (MGN180USAAP), complete to degree and order 180 (Konopliv et al., 1999). Konopliv et al. (1999) described the resolution in the model gravity field by means of a global degree-strength map, which provides an estimate of the maximum spherical harmonic degree, below which there is discernable power in the local gravity field. In some regions, wavelengths as short as 300 km in the free-air gravity field are resolved. Thus, gravity data provide an additional constraint on models of corona formation, although the resolution may not be adequate for application to many smaller coronae.

Johnson and Richards (2003) estimated the peak free-air gravity anomalies of selected coronae (relative to the background regional gravity field). Due to the variation in degree-strength, estimates were only obtained for 112 coronae and not all topographic groups were equally well represented (Table 1). The peak anomalies range from −68 to 198 mgal, where peak indicates maximum departure, positive or negative, from the background. For most of the topographic groups, both positive and negative peak free-air gravity anomalies are observed. Group 8 (depression) coronae, however, show uniformly negative peak free-air gravity anomalies, and Group 3a (rim surrounding interior high) coronae show only positive peak free-air gravity anomalies.

In our experiments negative free-air gravity anomalies develop over downwellings, becoming more negative with increasing time. For central downwelling a peripheral high in the free-air gravity is typically of small amplitude. For central upwelling, a positive free-air gravity anomaly in the central region may have amplitude comparable to, or in some cases greater than, the negative anomaly over the downwelling. Variability in amplitude of free-air gravity can be explained by the presence of a deforming crustal layer and variation in its thickness produced by deformation. In contrast to model topography, however, the free-air gravity anomaly is always negative over a downwelling. Thus, observations that show positive gravity anomalies over the centre of coronae imply central upwelling in light of this model. Because the anomaly caused by the de-

forming crustal layer generally acts in the opposite direction to that caused by the downwelling mantle, the largest gravity anomalies are calculated when there is no crustal layer (e.g. Figs. 3e–3f), and the smallest are calculated for a thick crust (e.g. Figs. 8e–8f). With crustal thickness ratios in the expected range of 1/6–1/3, however, significant variability in the amplitude of free-air gravity anomalies can also be attributed to variations in the relative viscosity of the crustal layer (e.g. Figs. 4e–4f, 5e–5f, 6e–6f).

The range of scaled peak free-air gravity estimates obtained from the numerical experiments overlaps generally with the range of observed gravity anomaly amplitudes (Table 1), which are typically on the order of 50 mgal, and occasionally as much as 200 mgal. In general, however, our scaled examples predict smaller gravity anomalies than are observed. We obtained anomalies greater in amplitude than 100 mgal, only when the crustal layer is absent (e.g. Figs. 3e and 3f). The gravity anomalies of observed Group 8 (depression) coronae (average −35 mgal) clearly imply central downwelling, but the relatively modest amplitude also implies that a low-density crust is present, reducing the amplitude of the anomalies relative to what would be observed in the absence of a crust (e.g. Fig. 3). Average gravity anomaly amplitudes for most of the other topographic groups are smaller than the standard deviation for that group of measurements. Thus we should be cautious in interpreting data that appear to be noisy. Only for Group 3a (rim surrounding high) does the average peak anomaly (64 mgal) differ significantly from zero, and clearly imply that a central upwelling mechanism is responsible for that group of corona.

As with the topographic anomalies, time dependence, and the scaling constants h and $\Delta\rho$, directly and proportionally influence the predicted gravity anomalies (12). Although we might predict gravity anomalies of greater magnitude by increasing the scaling constant h, the implied corresponding increase to model corona radius and topographic amplitude would not be consistent with observations. Alternative explanations for our calculation of smaller model anomalies than are observed could lie in inadequate resolution of the gravity field, or in our omission of possible deep-sourced anomalies (e.g. a mantle plume situated beneath the corona).

4.5. Gravity to topography ratio (GTR)

The shared dependence of gravity and topography anomalies on the scaling constant $h\Delta\rho$ suggests another measure independent of these scaling constants: the ratio of the peak amplitude of free-air gravity anomaly to topography. This measure is less strongly dependent on time, because both anomalies increase approximately linearly with time. The gravity/topography ratio (*GTR*) thus should be more useful for constraining model parameters η_c', and m'.

We computed *GTR* for each experiment by dividing the peak gravity above the downwelling by the peak topography above the downwelling, retaining the sign of each measure. With no crustal layer, this ratio provides values between 30 and 80 mgal km^{-1} for central downwelling, and between 30 and 65 mgal km^{-1} for central upwelling. The computed

GTR values are shown in Fig. 10 for calculations with different crust/lithosphere thickness (m') and viscosity (η_c') ratios, and either central downwelling (Figs. 10a–10c) or upwelling (Figs. 10d–10f). The spread of the measurements (from ∼9 distinct time levels for each experiment) shows that the *GTR* calculation removes most of the time-dependence inherent in each of the separate gravity and topography measures. Values of *GTR* show an almost linear dependence on the logarithm of η_c', for all values of m' examined. The range of *GTR* computed numerically varies between approximately −250 and +190 mgal km^{-1}. Similar values of *GTR* are obtained for central downwelling and upwelling models, other parameters being equal. The predictions of comparable models with a rigid upper boundary are similar, although amplitudes of *GTR* are typically reduced by a factor between ∼1.7 and 1.9.

For each m' examined, we find a value of η_c' (generally close to $\eta_c' = 1$) at which the *GTR* changes from negative to positive. This change in sign is driven by the change in sign of topography: for small η_c' crustal thickening causes elevated topography above a downwelling; for large η_c' flexure of the crust is downward above a downwelling (Fig. 10).

The average observed *GTR* values (Table 1) fall in the range of ±50 mgal km^{-1}, but individual coronae range from −280 to +150 mgal km^{-1}. For only two of the groups is the average *GTR* value clearly greater than the standard deviation of the measurements, and therefore probably significant. Group 3a (rim surrounding interior high) has an average *GTR* value of 46 ± 23 mgal km^{-1}. Its positive central gravity anomalies clearly indicate central upwelling. Therefore, using Figs. 10d–10f, a *GTR* of 46 mgal km^{-1} can be explained either by a relatively thick crust ($m' \sim 1/2$) whose viscosity is similar to that of the mantle, or by a thinner crust (1/6–1/3) whose viscosity is ∼5 times greater than that of the mantle. The amplitudes of the peak gravity (average 64 mgal) and topography anomalies (average 1.27 km), however, favour the thinner stronger crust (e.g. Figs. 5d and 5f). For the lithospheric thickness of 50 km that we inferred from coronae radii measurements, the implied crustal thickness is therefore in the range 10–20 km.

Estimates of *GTR* for Group 8 coronae (depressions) also appear significant at 38 ± 26 mgal km^{-1}, and in fact have a similar amplitude to those of Group 3a. The difference here is that gravity and topography have negative amplitude in the central region, implying that a central downwelling model is required (e.g. Figs. 5c and 5e). Figs. 10a–10c then shows that the observed *GTR* can be explained by approximately the same combinations of crustal thickness ratio and crustal viscosity ratio inferred for Group 3a.

The variability of the observed gravity/topography ratios for venusian coronae might also suggest spatial variation of the viscosity and thickness of the crust. Variability in crustal viscosity could result from variation in water content (e.g. Mackwell and Kohlstedt, 1993; Mackwell et al., 1998) as much as temperature (e.g. Karato et al., 1986). The uncertainties of the observed *GTR* measurements are sufficiently great, however, that any systematic variation either between or within coronae topographic groups is not yet evident.
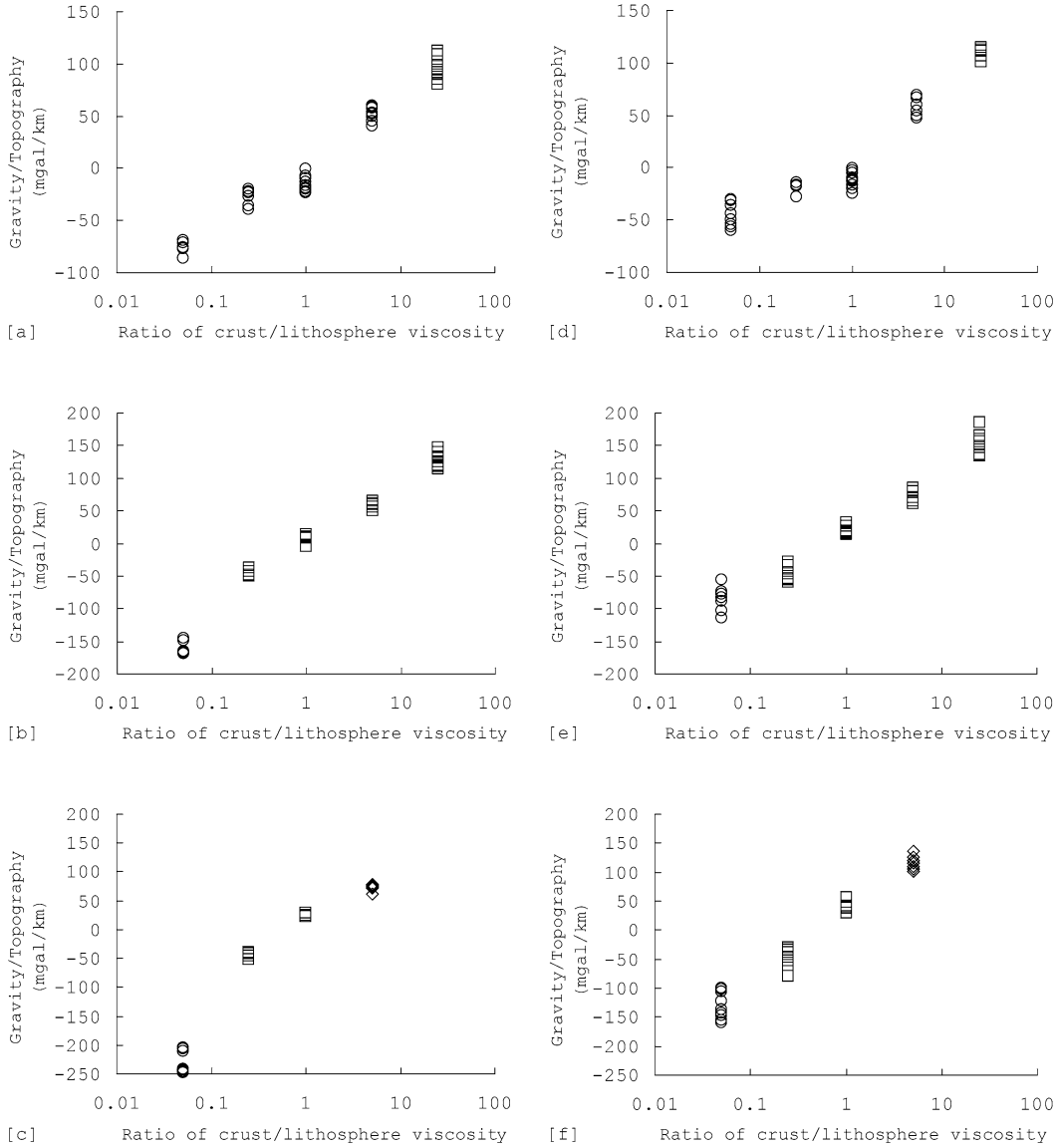
Fig. 10. Gravity to topography ratio (*GTR*), versus crust/lithosphere viscosity ratio η'_c, at a range of times in the numerical experiments with central downwelling (a–c) or central upwelling (d–f), free-slip upper boundary and initial crust/lithosphere thickness ratio $m' = 1/6$ (a,d), 1/3 (b,e), and 1/2 (c,f). Symbols show wavenumber: circles for $k = 1.277$, squares for $k' = 2.554$, and diamonds for $k' = 3.831$ ($R_0 = 3, 1.5$, and 1, respectively, for central downwelling).

4.6. Viscosity of the lithosphere

The hypothesis that R–T instability acting on a thermally controlled density stratification is the driving mechanism for corona formation, implies a timescale from which we infer an upper bound on the lithospheric viscosity (e.g. Neil and Houseman, 1999). If density depends only on temperature, then thermal conduction acts on the initial perturbation on a timescale of order ~20 Myr, and may cause density gradients to diffuse away rather than be amplified by the induced flow (Houseman and Molnar, 2001). Therefore, we assume that the growth of the instability takes less than ~20 Myr.

The growth time of the instability in our experiments, from the initial 1% perturbation, is in the range of 10–15 dimensionless time units (e.g. Fig. 3), at the wavenumber of maximum growth rate. The dimensional growth time is found by multiplying by t_0 (7). The resulting constraint that $15t_0 < \sim 20$ Myr

may be rewritten as a constraint on the viscosity parameter, η_m:

$$\eta_m < \sim gh\Delta\rho(2 \times 10^{13} \text{ s}), \tag{13}$$

where the numerical factor includes the conversion from Myr to seconds. Assuming the values of $h\Delta\rho = 3 \times 10^6$ kg m^{-2} inferred above from topography amplitude data, the viscosity of the mantle lithosphere is at most $\sim 5 \times 10^{20}$ Pa s and the crustal viscosity for $\eta'_c \sim 5$ (inferred from *GTR* analysis) is $\sim 3 \times 10^{21}$ Pa s. Although some uncertainty in $h\Delta\rho$ is possible, increasing or decreasing it by a factor of two would make it difficult to reproduce the observed range of gravity and topography anomalies.

This upper bound on lithospheric mantle viscosity ($\sim 5 \times 10^{20}$ Pa s) is comparable to viscosities previously inferred for the Venusian upper mantle. Nimmo and McKenzie (1996) estimated 3×10^{20} Pa s ($\pm$a factor of ~3) for the viscosity of the mantle using observations of gravity and topography over inter-

preted mantle plumes. Solomatov and Moresi (1996) estimated 10^{20}–10^{21} Pa s for the convecting mantle based on stagnant lid convection models with a temperature-dependent viscosity. Our inference that lithospheric mantle viscosity is less than $\sim 5 \times 10^{20}$ Pa s suggests that previous estimates of venusian mantle viscosity are too high—at least in regions where coronae have formed. While the venusian lithosphere may generally be much stronger than 5×10^{20} Pa s, this corona formation mechanism could still apply where lithospheric mantle viscosity is locally reduced by thermal or tectonic activity, as has been argued for terrestrial orogens (e.g. Billen and Houseman, 2004).

The 20 Myr timescale assumed in this model is much shorter than the inferred average age of the surface (e.g. 500 Myr (Phillips et al., 1992) or 750 Myr (McKinnon et al., 1997)). Thus, coronae could have formed at any time during the period preserved by the geological record. We cannot exclude the possibility, however, that the instability is driven by an unstable compositionally dense layer and not by thermally induced density differences. In that case the relevant upper limit on the time required for corona development could be as great as the inferred age of the surface, implying that the upper bound on viscosity of the mantle lithosphere could be 25–50 times greater than the value inferred from (13).

5. Conclusions

The numerical experiments described in this paper explore the hypothesis that Rayleigh–Taylor (R–T) instability of the mantle lithosphere is the mechanism by which coronae have formed on Venus. Axisymmetric R–T instability can produce the scale of uplift and most of the topographic forms displayed by coronae. A central upwelling mechanism is inferred for some coronae, whereas central downwelling is required for others. The sign of topography is not diagnostic of central upwelling or downwelling because crustal thickness variations induced by the deformation may cause a topographic high above a downwelling or a low above an upwelling when the opposite would be observed in the absence of a crustal layer. The model calculations show, however, that the gravity anomaly is always negative above a downwelling, although its amplitude may be diminished by deformation of the crust. Thus the sign of the gravity anomaly, in principle, is diagnostic of whether the corona is produced by central upwelling or by central downwelling. In practice it may be difficult to get sufficiently well resolved gravity data to apply this criterion to a particular corona.

The ratio of gravity to topography amplitude (*GTR*) shows a clear dependence on the ratio of crust to mantle viscosity, and a secondary dependence on the ratio of crust to mantle thickness. In particular, positive *GTR* values are found if the crust is very thin, or if it is stronger than the mantle; negative values are found if the crust is weak. For two groups of coronae (rim surrounding interior high, and depression) the observed *GTR* ($\sim$40 mgal km^{-1}) implies that a low density-crust is present, and that it is likely to be stronger than the lithospheric mantle by a factor of between 1 and $\sim$5, depending on the crustal thickness ratio m'. The amplitudes of peak gravity anomalies are more consistent with thinner crust (in the range say $1/6 < m' < 1/3$) for which the crustal viscosity contrast is closer to 5 than 1. The average observed radii of corona deformation imply a mantle lithosphere that is on average $\sim$50 km thick. Thus the implied crustal thickness is on the order of 10–20 km where these types of coronae have formed. The variation of observed *GTR* may imply that the local gravity field is not adequately resolved for the purpose of this analysis, but it may also suggest spatial variability in the relative viscosity and thickness of the crust.

References

Arvidson, R.E., Greeley, R., Malin, M.C., Saunders, R.S., Izenberg, N., Plaut, J.J., Stofan, E.R., Shepard, M.K., 1992. Surface modifications of Venus as inferred from Magellan observations of plains. J. Geophys. Res. 97, 13303–13318.

Billen, M.I., Houseman, G., 2004. Lithospheric instability in obliquely convergent margins: San Gabriel Mountains, S. California. J. Geophys. Res. 109, doi:10.1029/2003JB002605. B01404.

Chandrasekhar, S., 1961. Hydrodynamic and Hydromagnetic Stability. Clarendon Press, Oxford, UK.

Conrad, C.P., Molnar, P., 1997. The growth of Rayleigh–Taylor type instabilities in the lithosphere for various rheological and density structures. Geophys. J. Int. 129, 95–112.

Copp, D.L., Guest, J.E., Stofan, E.R., 1998. Stratigraphy of six coronae on Venus: Implications for timing and sequence of corona formation. J. Geophys. Res. 103, 19410–19418.

Grimm, R.E., Hess, P.C., 1997. The crust of Venus. In: Bougher, S.W., Hunten, D.M., Phillips, R.J. (Eds.), Venus II. Univ. of Arizona Press, Tucson, pp. 1205–1244.

Hansen, V.L., 2003. Venus diapirs: Thermal or compositional? GSA Bull. 115 (9), 1040–1052.

Hoogenboom, T., Smrekar, S.E., Anderson, F.S., Houseman, G.A., 2004. Admittance survey of Type 1 coronae on Venus. J. Geophys. Res. Planets 109 (E3), doi:10.1029/2003JE002171. E03003.

Houseman, G.A., Molnar, P., 1997. Gravitational (Rayleigh–Taylor) instability of a layer with non-linear viscosity and convective thinning of continental lithosphere. Geophys. J. Int. 128, 125–150.

Houseman, G.A., Molnar, P., 2001. Mechanisms of lithospheric rejuvenation associated with continental orogeny. In: Miller, J.A., Holdsworth, R.E., Buick, R.E., Hand, M. (Eds.), Continental Reactivation and Reworking. In: Special Publications, vol. 184. Geological Society of London, London, pp. 13–38.

Houseman, G.A., Barr, T.D., Evans, L., 2002. Diverse geological applications for basil: A 2D finite deformation computational algorithm. In: 27th General Assembly of the European Geophysical Society. Geophys. Res. Abstr. 4. No. EGS02-A-05321.

Janes, D.M., Squyres, S.W., Bindschadler, D.L., Baer, G., Schubert, G., Sharpton, V.L., Stofan, E.R., 1992. Geophysical models for the formation and evolution of coronae on Venus. J. Geophys. Res. 97, 16055–16067.

Johnson, C.L., Richards, M., 2003. A conceptual model for the relationship between coronae and large-scale mantle dynamics on Venus. J. Geophys. Res. 180 (E6), doi:10.1029/2002JE001962. 5058.

Jordan, T.H., 1978. Composition and development of continental tectosphere. Nature 274, 544–548.

Karato, S.I., Paterson, M.S., Fitzgerald, J.D., 1986. Rheology of synthetic olivine aggregates—Influence of grain size and water. J. Geophys. Res. 91, 8151–8176.

Kaula, W.M., 1999. Constraints on Venus evolution from radiogenic argon. Icarus 139, 32–39.

Kaula, W.M., Phillips, R.J., 1981. Quantitative tests for plate tectonics on Venus. Geophys. Res. Lett. 8, 1187–1190.

Koch, D.M., Manga, M., 1996. Neutrally buoyant diapirs: A model for Venus coronae. Geophys. Res. Lett. 23 (3), 225–228.

Konopliv, A.S., Banerdt, W.B., Sjogren, W.S., 1999. Venus gravity: 180th degree and order model. Icarus 134, 3–18.

Mackwell, S.J., Kohlstedt, D.L., 1993. High temperature deformation of diabase: Implications for tectonics on Venus. EOS Trans. Am. Geophys. Union Suppl. 74, 378.

Mackwell, S.J., Zimmerman, M.E., Kohlstedt, D.L., 1998. High temperature deformation of dry diabase with application to tectonics on Venus. J. Geophys. Res. 103, 975–984.

Malvern, L.E., 1969. Introduction to the Mechanics of a Continuous Medium. Prentice–Hall.

McKenzie, D., 1977. Surface deformation, gravity anomalies and convection. Geophys. J. R. Astron. Soc. 48, 211–238.

McKinnon, W.B., Zahnle, K.J., Ivanov, B.I., Melosh, H.J., 1997. Cratering on Venus: Models and observations. In: Bougher, S.W., Hunten, D.M., Phillips, R.J. (Eds.), Venus II. Univ. of Arizona Press, Tucson, pp. 969–1014.

Molnar, P., Houseman, G.A., 2004. The effects of buoyant crust on the gravitational instability of thickened mantle lithosphere at zones of intracontinental convergence. Geophys. J. Int. 158, 1134–1150, doi:10.1111/j.1365-246X.2004.02312.x.

Molnar, P., Houseman, G.A., Conrad, C.P., 1998. Rayleigh–Taylor instability and convective thinning of mechanically thickened lithosphere: Effects of non-linear viscosity decreasing exponentially with depth and of horizontal shortening of the layer. Geophys. J. Int. 133, 568–584.

Neil, E.A., Houseman, G., 1999. Rayleigh–Taylor instability of the upper mantle and its role in intraplate orogeny. Geophys. J. Int. 138, 89–107.

Nimmo, F., McKenzie, D., 1996. Modelling plume related melting, uplift and gravity on Venus. Earth Planet. Sci. Lett. 145, 109–123.

Pettengill, G.H., Ford, P.G., Johnson, W.T.K., Raney, R.K., Soderblom, A.K., 1991. Magellan: Radar performance and data products. Science 252, 260–265.

Phillips, R.J., 1990. Convection driven tectonics on Venus. J. Geophys. Res. 95, 1301–1316.

Phillips, R.J., Malin, M.C., 1983. The interior of Venus and tectonic implications. In: Hunten, D.M., Colin, L., Donahue, T.M., Moroz, V.I. (Eds.), Venus. Univ. Arizona Press, Tucson, pp. 159–214.

Phillips, R.J., Herrick, R.R., Grimm, R.E., Raubertas, R.F., Sarkar, I.C., Arvidson, R.E., Izenberg, N., 1992. Impact crater distribution on Venus: Implications for planetary resurfacing. J. Geophys. Res. 97, 15923–15948.

Poudjom-Djomani, Y., O'Reilly, S.Y., Griffin, W.L., Morgan, P., 2001. The density structure of sub-continental lithosphere through time. Earth Planet. Sci. Lett. 184, 605–621.

Pysklywec, R.N., Beaumont, C., 2004. Intraplate Tectonics: Feedback between radioactive thermal weakening and crustal deformation driven by mantle lithosphere instabilities. Earth Planet. Sci. Lett. 221, 275–292.

Smrekar, S.E., Stofan, E.R., 1997. Corona formation and heat loss on Venus by coupled upwelling and delamination. Science 277, 1289–1294.

Solomatov, V.S., Moresi, L.N., 1996. Stagnant lid convection on Venus. J. Geophys. Res. 101, 4737–4753.

Solomon, S.C., Head, J.W., 1982. Mechanisms for lithospheric heat transport on Venus: Implications for tectonic style and volcanism. J. Geophys. Res. 87, 9236–9246.

Squyres, S.W., Janes, D.M., Baer, G., Bindschadler, D.L., Schubert, G., Sharpton, V.L., Stofan, E.R., 1992. The morphology and evolution of coronae on Venus. J. Geophys. Res. 97 (E8), 13611–13634.

Stofan, E.R., Bindschadler, D.L., Head, J.W., Parmentier, E.M., 1991. Corona structures on Venus: Models of origin. J. Geophys. Res. 94 (E4), 20933–20946.

Stofan, E.R., Sharpton, V.L., Schubert, G., Baer, G.D., Bindschadler, D.L., Janes, D.M., Squyres, S.W., 1992. Global distribution and characteristics of coronae and related features on Venus: Implications for origin and relation to mantle processes. J. Geophys. Res. 97, 13347–13378.

Tackley, P.J., Stevenson, D.J., 1991. The production of small venusian coronae by Rayleigh–Taylor instabilities in the uppermost mantle. Eos Trans. Am. Geophys. Union 72, 287.

Tackley, P.J., Stevenson, D.J., Scott, D.R., 1992. Volcanism by melt driven Rayleigh–Taylor instabilities and possible consequences of melting for admittance ratios on Venus. LPI Contribution 789.

Turcotte, D.L., Schubert, G., 2002. Geodynamics. Cambridge Univ. Press.

Whitehead, J.A., Luther, D.S., 1975. Dynamics of laboratory diapir and plume models. J. Geophys. Res. 80, 705–717.

Yamada, Y., Ito, K., Yokouchi, Y., Tomano, T., Ohtsubo, T., 1975. Finite element analysis of steady fluid and metal flow. In: Gallagher, R.H., Oden, J.T., Taylor, C., Zienkiewicz, O.C. (Eds.), Finite Elements in Fluids, vol. 1. Wiley, New York, pp. 73–94.

Zhong, S., Gurnis, M., Moresi, L., 1996. Free-surface formulation of mantle convection. 1. Basic theory and application to plumes. Geophys. J. Int. 127, 708–718.